catalysts

MDPI

Article

Synthesis of Nanocrystalline Metal Tungstate $NiWO_4/CoWO_4$ Heterojunction for UV-Light-Assisted Degradation of Paracetamol

Fahad Ahmed Alharthi *, Alanoud Abdullah Alshayiqi, Wedyan Saud Al-Nafaei, Adel El Marghany, Hamdah Saleh Alanazi and Imran Hasan *

Department of Chemistry, College of Science, King Saud University, Riyadh 11451, Saudi Arabia
* Correspondence: fharthi@ksu.edu.sa (F.A.A.); iabdulateef@ksu.edu.sa (I.H.)

Abstract: The discharge of pharma products such as paracetamol (PCT) into water has resulted in great harm to humans and emerged as a potential threat requiring a solution. Therefore, the development of smart and efficient materials as photocatalysts has become imperative in order to treat PCT in wastewater. The present study demonstrates the synthesis of pristine $NiWO_4$ and $CoWO_4$ and a heterojunction nanostructure, $NiWO_4/CoWO_4$, through a hydrothermal process using a Teflon-lined autoclave at 180 °C for 18 h. Various spectroscopic techniques, such as X-ray diffraction (XRD), Fourier transform infrared (FTIR), ultraviolet–visible (UV–Vis), transmission electron microscopy (TEM), scanning electron microscopy–energy dispersive X-ray (SEM–EDX), and X-ray photoelectron spectroscopy (XPS) were utilised to determine the lattice, structural, optical, and morphological information of the solid nanomaterial upon heterojunction formation. The synthesised nanomaterials were exploited for the photocatalytic degradation of paracetamol (PCT) under UV light irradiation. Photocatalytic experiments were performed for the optimization of various reaction parameters, such as irradiation time, pH, catalyst dose, and PCT concentration at room temperature. The results obtained suggested that the heterojunction nanocomposite $NiWO_4/CoWO_4$ exhibited enhanced photocatalytic efficiency (97.42%) with PCT as compared to its precursors—96.50% for $NiWO_4$ and 97.12% for $CoWO_4$. The photocatalytic data were best defined by the Langmuir–Hinshelwood (L–H) model of pseudo-first-order kinetics, with apparent rates constant at 0.015 min^{-1} for $NiWO_4$, 0.017 min^{-1} for $CoWO_4$, and 0.019 min^{-1} for $NiWO_4/CoWO_4$ NC. It was observed that $NiWO_4/CoWO_4$ NC with enhanced optical properties effected a higher rate of PCT degradation due to the improved bandgap energy upon heterojunction formation. The scavenger test revealed the involvement of $^{\bullet}OH$ radicals as reactive oxidant species (ROS) in PCT degradation. The material was found to be highly stable and reusable for the degradation of PCT at optimized reaction conditions.

Keywords: heterojunction; nanocomposites; tungstate; photocatalytic degradation; pharmaceuticals

check for updates

Citation: Alharthi, F.A.; Alshayiqi, A.A.; Al-Nafaei, W.S.; El Marghany, A.; Alanazi, H.S.; Hasan, I. Synthesis of Nanocrystalline Metal Tungstate $NiWO_4/CoWO_4$ Heterojunction for UV-Light-Assisted Degradation of Paracetamol. *Catalysts* **2023**, *13*, 152. https://doi.org/10.3390/catal13010152

Academic Editor: Meng Li

Received: 20 December 2022
Revised: 3 January 2023
Accepted: 5 January 2023
Published: 9 January 2023

1. Introduction

In recent years, pharmaceutical products, personal care products (PPCs), and pesticides in water bodies have been categorized as contaminants of emerging concern (CECs) [1]. Among these emerging pollutants, pharma products have begun to gain researchers' attention owing to their toxic influence on human health [2]. One of these pharma products, paracetamol (PCT), also known as acetaminophen, is widely used in analgesic and antipyretic drugs for treating headache, fever, etc. [3]. The high consumption of the drug during COVID-19 has resulted in a harmful impact on ecology and human health through its presence in wastewater effluents [4]. The main sources of PCT inclusion into the aquatic system are the pharmaceutical industry and the excretory waste of both humans and animals who have received medical treatment [4,5]. With each successive year, PCT concentrations in lakes and rivers have significantly increased, which can cause diseases such as liver failure, hepatic necrosis, nephrite toxicity, and possibly death [6,7].

Therefore, to address this issue, there is a need to develop efficient methods and technology to treat PCT from wastewater streams.

There are numerous methods reported in the literature for removing these pollutants from the environment, such as electrochemical separation, liquid extraction, chemical oxidation, membrane separation, biodegradation, and adsorption technology [8–10]. However, sludge formation, slow procedures, and mass transfer properties from one phase to another make these methods less efficient. Therefore, an advanced oxidation process (AOP) in association with photocatalytic degradation was taken into consideration for the treatment of these PPCPs. Due to its lack of toxicity, affordability, lack of mass transfer limitations, chemical stability, and potential operation at room temperature, photocatalytic oxidation has emerged as one of the most efficient and innovative technologies to trigger pharma pollutants without causing secondary waste to enter the environment [11]. The technology utilizes the irradiation of a catalyst material using solar energy, and depending on its optical properties, generates reactive oxidant species (ROS), hydroxy ($^{\bullet}OH$), or superoxide ($^{\bullet}O_2^{-}$) radicals, which are responsible for mineralization process [12].

Based on their high aspect ratio, smaller size, and good optical properties, nanomaterials have been identified as the most effective and potentially useful materials to address this sustainability issue, offering some fundamental and practical approaches for wastewater treatment operations [13]. Among these nanomaterials, semiconductor metal oxides, such as zirconia (ZrO_2), zinc oxide (ZnO), titanium dioxide (TiO_2), iron (III) oxide (Fe_2O_3), tungsten trioxide (WO_3), and vanadium (V) oxide (V_2O_5), etc., have been proved to be promising photocatalysts for wastewater treatment processes due to their excellent physicochemical properties [8,14–17]. The nanostructured metal tungstates with the empirical formula MWO_4 (M = Co, Zn, Sn, Ni, Mn etc.) have been recognized as materials with advanced photocatalytic activity, chemical stability, low cost, and non-toxicity [18]. They are associated with a wolframite monoclinic structure and appropriate band gap energy, which classifies them as exemplary materials for scientific and engineering applications such as conventional catalysis, scintillator materials, photoluminescence, optical fibers, microwave technology, supercapacitors, and semiconductors [18,19]. $NiWO_4$ is one of the members of the tungstate family with intriguing structural properties, large surface area, and photoluminescent characteristics, with an energy bandgap value of 2.97 eV [20]. However, rapid recombination of electron–hole pairs in pure substances restricts their photocatalytic activities, and to address this issue, the strategy of heterojunction formation was taken into consideration [21]. The heterojunction formation results in spatial separation of photogenerated electron–hole pairs, and thus enhances the photocatalytic activities [22]. In the present study, $CoWO_4$ was used for heterojunction formation with $NiWO_4$ through the hydrothermal process. CoWO4, with an energy bandgap value of 2.8 eV, exhibits excellent photocatalytic activities [23]. The resultant nanostructured $NiWO_4/CoWO_4$ heterojunction was used as a catalyst for photocatalytic degradation of paracetamol under mercury lamp (Ultraviolet radiation) in photocatalytic reactor. Various reaction factors influencing the degradation process, such as PCT concentration, irradiation time, pH, and amount of catalyst, were optimized. The novelty of this work lies in the use of mixed metal tungstate heterojunction ($MWO_4/M'WO_4$) nanomaterials in photocatalytic degradation processes to remove pharmaceuticals from wastewater.

2. Results and Discussion

2.1. Material Characterization

2.1.1. FTIR Analysis

The FTIR spectrum of the prepared metals and mixed metal tungstate catalysts is shown in Figure 1. In the FTIR spectra of Figure 1a,b, 466 and 456 cm^{-1} belong to Ni–O and Co–O bonds, 537 and 523 cm^{-1} belong to Ni–O–W and Co–O–W bonds, 618 belongs to the W–O bonds, 700–880 cm^{-1} belongs to the W–O stretching mode of the WO_4 tetrahedron, W–O–W bond vibrational modes [24–26]. The –OH group stretching and bending vibrations as a result of moisture adsorption appeared at 3427–3446 cm^{-1} and

1635–1640 cm^{-1} [27]. The FTIR spectra of heterojunction $NiWO_4/CoWO_4$ NC Figure 1c exhibit most of the peaks from $NiWO_4$ and $CoWO_4$, but with some shifted values, which suggest that in the wolframite monoclinic structure, both Co and Ni took the lattice position in the solid structure.

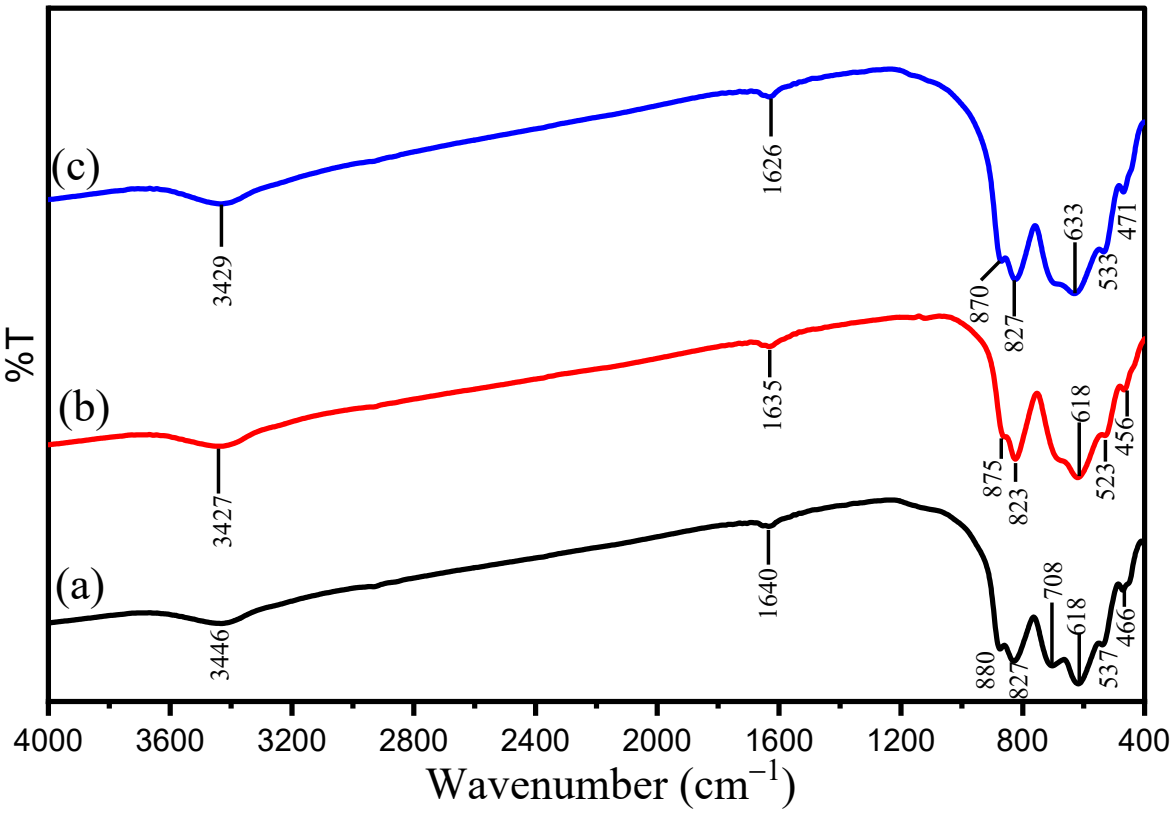

Figure 1. FTIR spectra of (**a**) $NiWO_4$ (**b**) $CoWO_4$ and (**c**) mix metal tungstate $NiWO_4/CoWO_4$ NC.

2.1.2. X-ray Diffraction (XRD)

The crystal structures of the prepared metals and mixed metal tungstate catalysts were identified by X-ray diffraction (XRD) patterns. Figure 2 shows the XRD pattern of the catalysts synthesized through a typical reaction. The XRD spectra of $CoWO_4$ show characteristic peaks at 2θ value of 2.37°, 24.91°, 24.91°, 30.75°, 36.78°, 37.93°, 48.66°, 54.53°, 61.91°, and 65.21°, which belong to miller indices (100), (011), (110), (020), (002), (200), (022), (031), (310), and (040) respectively. The XRD spectra of $NiWO_4$ show characteristic peaks at 2θ value of 6.51°, 19.35°, 24.03°, 24.99°, 31.02°, 36.65°, 39.24°, 41.76°, 44.84°, 46.52°, 49.09°, 52.42°, 54.74°, 62.41°, 65.82°, and 69.10°, which belong to miller indices (010), (100), (011), (110), (111), (021), (200), (121), (112), (211), (022), (220), (130), (202), (113), (311), and (041) respectively. All reflection peaks can be indexed as the monoclinic crystal systems of $CoWO_4$ (JCPDS Card No. (96–317)) and $NiWO_4$ (JCPDS Card No. (96–278)). Finally, the XRD pattern of $NiWO_4/CoWO_4$ NC shows peaks ascribed to the $NiWO_4$ at 16.91° (010), 30.63° (111), 41.37° (121), 44.43° (112), 46.02° (211), 52.10° (202), 65.32° (311), and 68.82 (041), and peaks ascribed to the $CoWO_4$ at 30.81° (020), 36.32° (002), 54.25° (031), and 61.95° (310), respectively. Moreover, some peaks ascribed to both $NiWO_4$ and $CoWO_4$ show at 18.97° (100), 24.62° (011), 24.62° (110), 38.72° (200), and 48.78° (022), which suggests the successful formation of $NiWO_4/CoWO_4$ heterojunctions. For further information about the crystallite size and dislocation density, the Scherrer's equation was taken into consideration. The crystallite size and interlayer spacing were calculated using the Scherrer's Equation:

$$D = \frac{0.9\lambda}{\beta \cos \theta} \quad (1)$$

$$\text{Dislocation Density } (\delta) = \frac{1}{D^2} \tag{2}$$

$$\text{Interlayer Spacing } (d_{111}) = \frac{n\lambda}{2\text{Sin}\theta} \tag{3}$$

$$\%\text{Crystallinity } = \frac{\text{Area Under Crystalline Peaks}}{\text{Total Area}} \times 100 \tag{4}$$

where D is the crystallite size, λ is the characteristic wavelength of the X-ray, β represents angular width in radian at intensity equal to half of its maximum of the peak, and θ is the diffraction angle. The average particle size of $CoWO_4$, $NiWO_4$, and $NiWO_4/CoWO_4$ NC were 27.16, 22.16, and 19.07 nm, respectively, calculated using Equation (2). Moreover, from Table 1, it can be seen that the crystallinity of the heterojunction nanocomposite increased to 38% after heterojunction formation, suggesting a successful occupation of lattice sites by Co in the $NIWO_4$ solid structure without producing any impurity. The process reflected a contraction in particle size and an increase in dislocation density due to deformation in the solid lattice of $CoWO_4$ and $NiWO_4$.

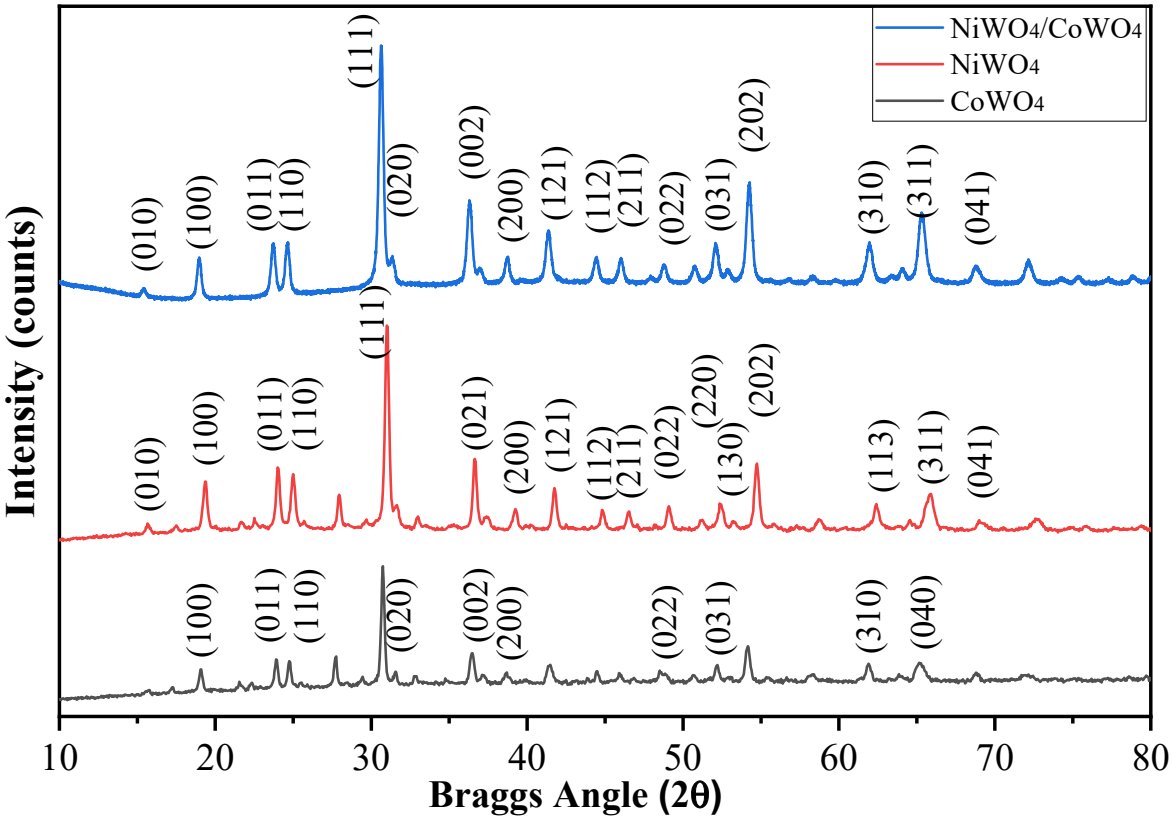

Figure 2. XRD pattern of ($CoWO_4$, $NiWO_4$, $NiWO_4/CoWO_4$ NC) nanomaterials.

Table 1. XRD parameter of $CoWO_4$, $NiWO_4$, and $NiWO_4/CoWO_4$ NC.

Component	2θ	FWHM (β_{hkl})	Interlayer Spacing (nm) at 2θ	Crystallite Size (nm) at 2θ	Dislocation Density (δ)×10^{15} Lines (m^{-2})	Crystallinity (%)
$CoWO_4$	30.748	0.26203	0.020414	27.16	1.35	23.60
$NiWO_4$	31.015	0.32392	0.020587	22.16	2.03	23.25
$NiWO_4/CoWO_4$ NC	30.64	0.36296	0.020344	19.07	2.75	38.14

2.1.3. Scanning Electron Microscopy (SEM)

The surface morphological changes in the material during the solid-state processes were observed using scanning electron microscopy (SEM). The SEM images of the sintered $NiWO_4$ taken at 10,000× magnification is shown in Figure 3a. The sample's morphology is porous. The complete coverage of the substrate is evident in the micrographs. These surfaces evince uneven surface morphology and irregular geometry quite clearly, while in the SEM image of $CoWO_4$ shown in the Figure 3b, the grain arrangements and sizes are irregular. Figure 3c presents a SEM image of $NiWO_4/CoWO_4$ NC, which shows large, irregularly sized grains. The EDX spectrum recorded for the sample, which is depicted in Figure 3d, was used to explore the elements present in the sample. The presence of the components Co, W, Ni, and O in the mixed metal tungstate $NiWO_4/CoWO_4$ NC was confirmed by the EDX analysis.

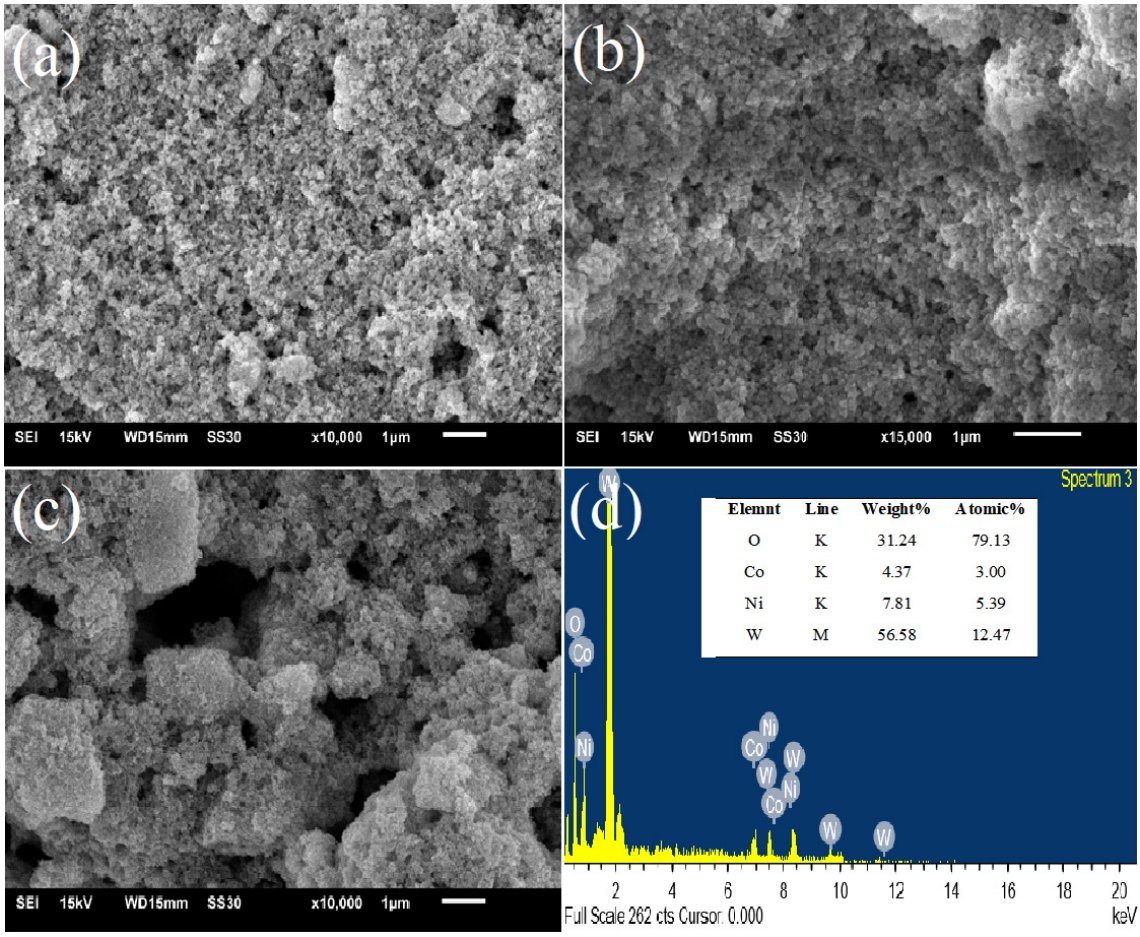

Figure 3. SEM images of the metal tungstate (**a**) $NiWO_4$; (**b**) $CoWO_4$, mix metal tungstate (**c**) $NiWO_4/CoWO_4$ NC; (**d**) EDX of $NiWO_4/CoWO_4$ NC.

2.1.4. Transmission Electron Microscopy (TEM)

The optimal diameter of the mix metal tungstate was determined using transmission electron microscopy (TEM), and further investigation was carried out to establish the crystallinity and morphology of the metal's tungstate. Figure 4a–c presents the TEM images of $NiWO_4$, $CoWO_4$, and $NiWO_4/CoWO_4$ NC synthesized nanoparticles, respectively, in which $NiWO_4$ shows rod-like morphology and $CoWO_4$ shows a mix of rod- and irregular-shaped particles, while after heterojunction, a new morphology appears for $NiWO_4/CoWO_4$ NC constituted of irregular-shaped particles with mitigated monoclinic structure (Figure 4d). The statistical gaussian distribution profile applied for average

particle size distribution suggested an average of 20 nm particle size for $NiWO_4/CoWO_4$ NC shown in the Figure 4e, which has been found to be in close agreement with the Scherer formula.

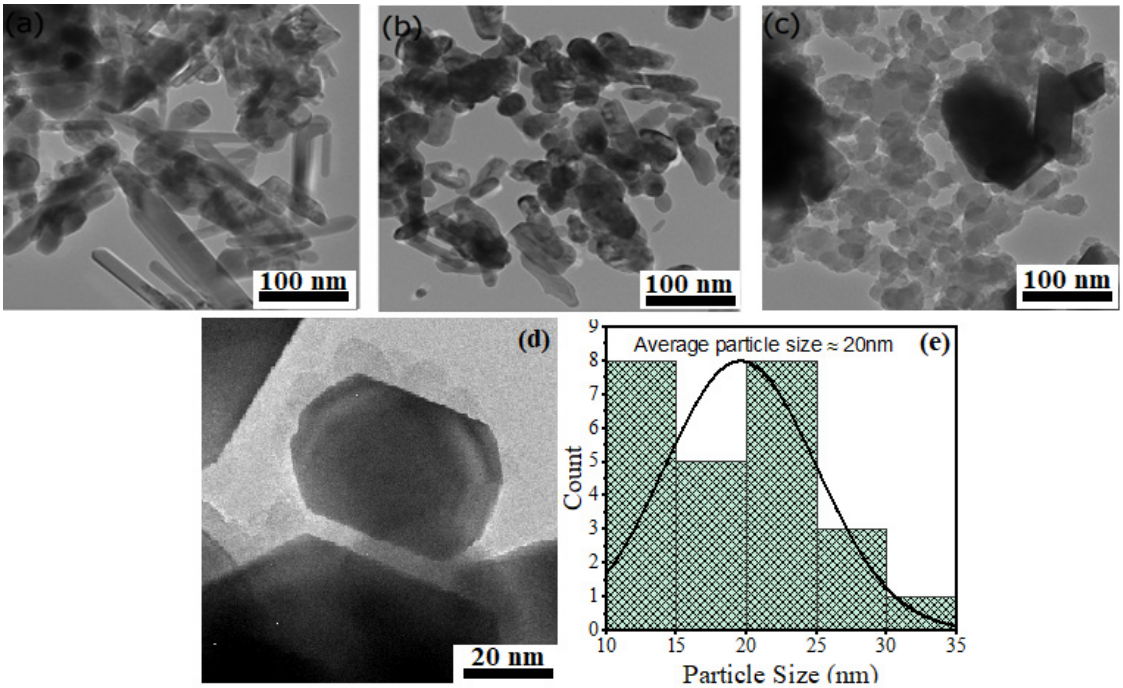

Figure 4. TEM images of the metal tungstates. (**a**) $NiWO_4$; (**b**) $CoWO_4$; (**c**) $NiWO_4/CoWO_4$ NC; (**d**) particle size distribution of $NiWO_4/CoWO_4$ NC; (**e**) statistical gaussian distribution profile for average particle size distribution.

2.1.5. UV/Vis Spectrophotometer

The produced catalyst's optical characteristics can be determined by UV–Vis spectroscopic studies, and the spectra are shown in Figure 5. The UV–vis spectrum has a broad line, which denotes absorption throughout the whole UV–Vis region. The existence of numerous consecutive energy levels in the photocatalyst was attributable to the broad absorption spectrum shown by Figure 5, in which the absorption maxima (λ_{max}) of $NiWO_4$, $CoWO_4$, and $NiWO_4/CoWO_4$ NC were observed around 263, 331, and 360 nm, respectively. The UV spectrum of $NiWO_4$ and $CoWO_4$ suggested the synthesized NPs were UV light-active only, while a broad spectrum from 200–650 nm in the case of $NiWO_4/CoWO_4$ NC suggested UV as well as visible light activity of the heterojunction. Thus, the formation of heterojunction results in enhancement of the light-absorption capacity of the material [28]. Tauc's relationship was used to determine the band gap using the absorption data:

$$(\alpha h\nu) = A(h\nu - E_g)^n \quad (5)$$

where α = absorption coefficient, h = plank constant, ν = frequency of radiations, A = constant, and n is a constant of transition variations depending on the type of electronic transition, i.e., n = 1/2 for direct transitions and n = 2 for the indirect transitions. Energy bandgap values were taken from the slope of a linear plot between $(\alpha h\nu)^2$ and E_g; the intercept give rise to the value of energy band gap. Tauc's plot specified the value of E_g as 3.04, 2.32, and 1.14 eV for the synthesized $NiWO_4$, $CoWO_4$, and $NiWO_4/CoWO_4$ NC, respectively. Thus, it is also quantitively proved that heterojunction formation results in contraction of the energy bandgap, and thus restricts the electron–hole pair recombination rate.

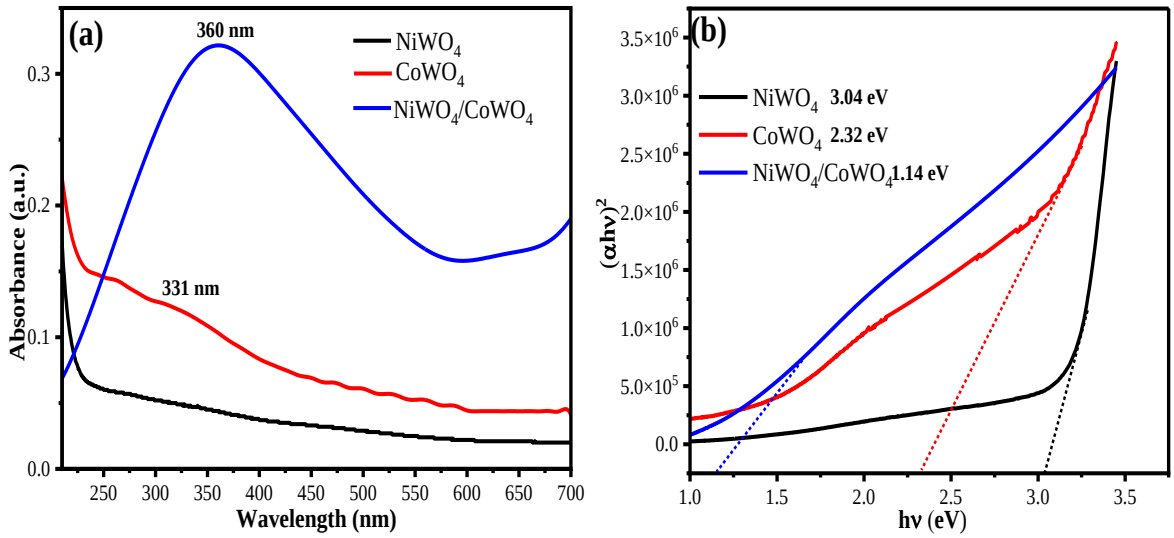

Figure 5. (**a**) UV–Vis plot of $NiWO_4$, $CoWO_4$, $NiWO_4/CoWO_4$ NC in wavelength range of 200–700 nm; (**b**) Tauc′s plot for the band gap energy (E_g) of the materials.

To further investigate the chemical oxidation state of the elements in the synthesized $NiWO_4/CoWO_4$ NC material, XPS analysis was taken into consideration. Figure 6a represents the XPS survey spectra of $NiWO_4/CoWO_4$ NC, which confirm the presence of W4f, O1s, Ni2p, and Co2p in the material. In order to observe the change in the oxidation states of elements during heterojunction formation, the deconvoluted spectres were studied. Figure 6b represents the deconvoluted XPS spectra of W4f, which show two peaks at 46.48 eV and 49.49 eV, corresponding to the $W4f_{7/2}$ and $W4f_{5/2}$ states associated with W^{6+} chemical state [29]. Figure 6c represents three deconvoluted peaks for O1s, corresponding to 538.44, 539.44, and 541.44 eV, associated with O1 (Co–O), O2 (W–O), and O3 (Ni–O) bonds [30,31]. The XPS spectra in Figure 6d for Co2P show two deconvoluted peaks at 868.01 and 872.78 eV associated with two states $Co2p_{3/2}$ and $Co2p_{1/2}$ states of Co^{2+}, respectively [32]. Similarly, Figure 6e, corresponding to the XPS spectra of Ni2p, represents the two states $Ni2p_{3/2}$ and $Ni2p_{1/2}$ for the Ni^{2+} chemical state at 884.94 eV and 890.87 eV [33]. The outcomes of the XPS studies clearly confirm the formation of heterojunction $NiWO_4/CoWO_4$ NC by the validation of the chemical stability of the Ni^{2+} and Co^{2+} ions in the lattice.

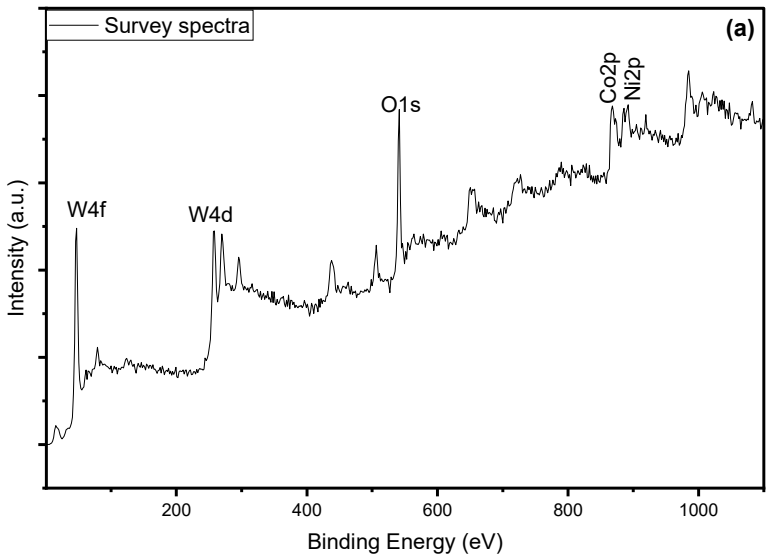

Figure 6. *Cont.*

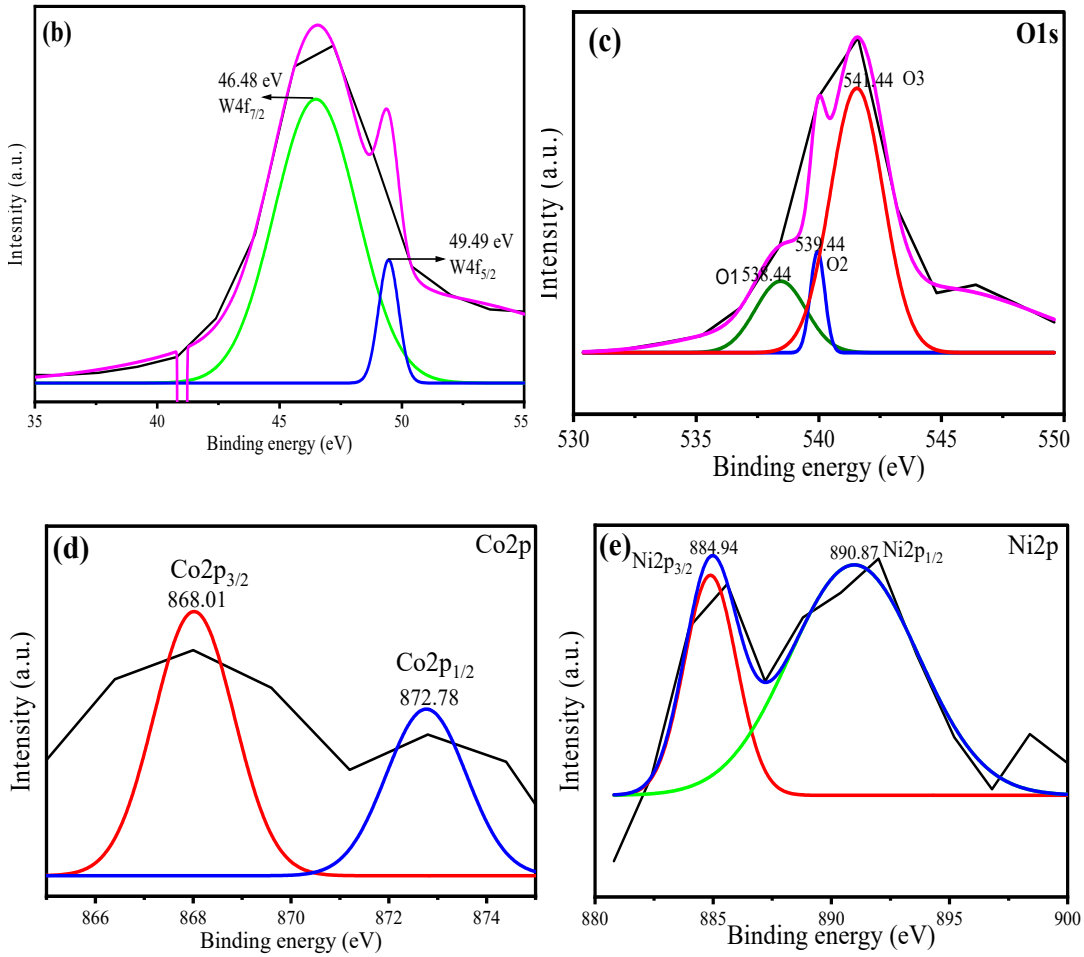

Figure 6. (**a**) XPS survey spectra of $NiWO_4/CoWO_4$ NC deconvoluted XPS spectra for (**b**) W4f, (**c**) O1s, (**d**) Co2p, and (**e**) Ni2P.

2.2. Photocatalysis and Optimization of Reaction Parameters

2.2.1. Photocatalysis with Variable Paracetamol Concentration

The photocatalytic experiments were performed at different PCT concentrations in the range of 5–60 ppm to observe the effect of PCT concentration on degradation rates using $NiWO_4$, $CoWO_4$, and $NiWO_4/CoWO_4$ NC. The results obtained are shown in Figure 7a–d, and suggest that over a span of 120 min of irradiation, the degradation efficiencies of the synthesized nanomaterials decreased with increasing paracetamol concentration. These findings were in close agreement with a number of studies, where the activation of the reaction by photon absorption was often the initial step [34]. Another explanation for the result shown in Figure 7 is that the formation of radicals and holes under irradiation remained consistent and sufficient for the breakdown of paracetamol at low concentrations, while at high concentrations, screening hindered their path towards the catalyst surface, which led to a decrease in the paracetamol degradation rate [35]. Acceptable degradation rates were obtained up to 50 ppm PCT concentration, which was used in further photocatalytic experiments.

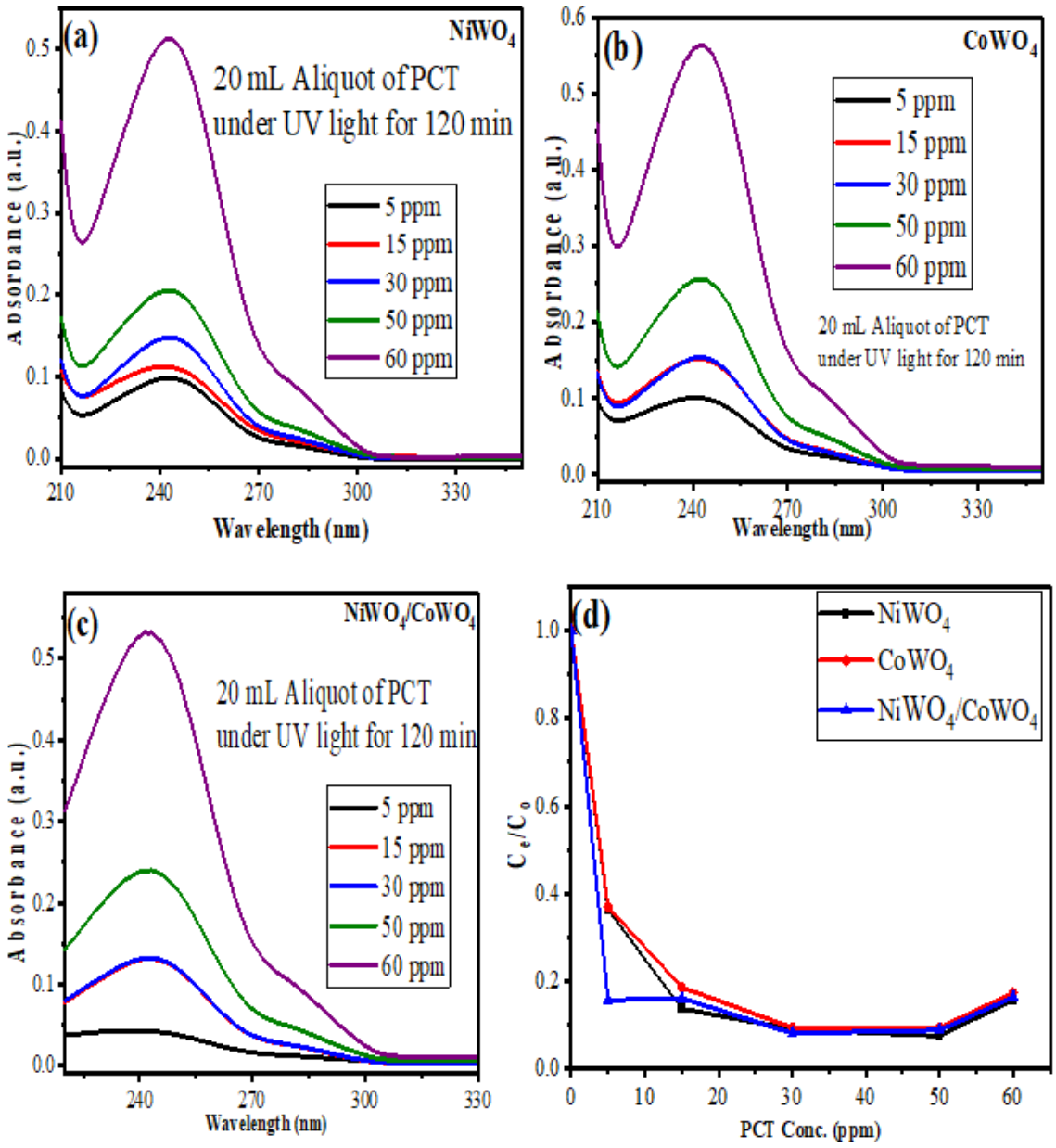

Figure 7. Effect of variable PCT concentration (5–60 ppm) using 5 mg prepared (**a**) $NiWO_4$, (**b**) $CoWO_4$, (**c**) $NiWO_4/CoWO_4$ NC, and (**d**) C_e/C_o vs. PCT conc. Plot.

2.2.2. Photocatalysis with Variable Catalyst Dosage

The photodegradation of paracetamol under irradiation is shown in Figure 8a–d as a function of catalyst dosage at 5, 10, 15, and 20 mg. Additionally, the other reaction conditions remained the same. As observed in Figure 8, the results showed that the degradation rate decreased by 15–20 mg with the addition of more catalyst. The number of active sites that could absorb additional photons rose as the catalyst dosage was raised. However, the increase in catalyst dose appeared to result in an excess dosage, which produced suspension turbidity in the solution. The efficiency of the photocatalytic process also declined as a result of the lower light penetration [36,37]. After 2 h of irradiation with the 10 mg catalyst dosage was taken as optimum for further experiments.

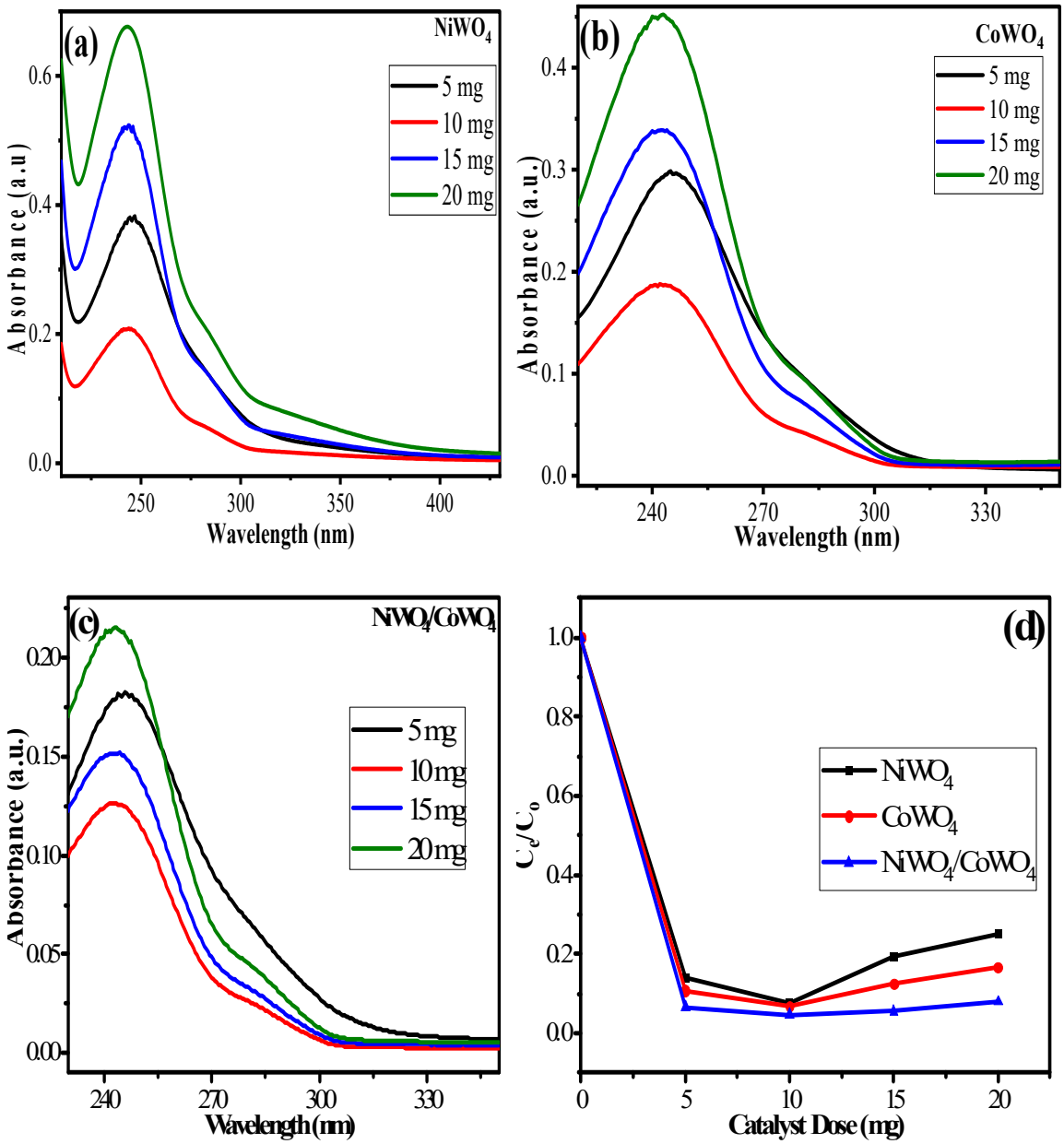

Figure 8. Effect of variable catalyst dose (5–20 mg) using 50 ppm PCT for (**a**) $NiWO_4$, (**b**) $CoWO_4$, (**c**) $NiWO_4/CoWO_4$ NC, and (**d**) C_e/C_o vs. catalyst dose plot.

2.2.3. Photocatalysis with Variable Paracetamol Solution pH

The pH is an important parameter in photochemical reactions. The results, which are presented in Figure 9, demonstrate how the effects of pH on the paracetamol degradation were investigated at various pH ranges from 3 to 10 in order to determine the ideal pH for the degradation process. This study included three catalysts ($NiWO_4$, $CoWO_4$, and $NiWO_4/CoWO_4$ NC), which were studied separately. The particle surface was positively charged at pH levels below 5, and negatively charged at pH levels above 5. Additionally, paracetamol has a pKa value of 9.38, making it a weak base. In light of this, the adsorption–desorption characteristics of the catalyst surface are significantly influenced by the pH value [34]. The results presented in Figure 8 show that the degradation rate rose as the pH value rose. This can be ascribed to increased hydroxide ion creation, because at high pH, more hydroxide ions that are already present on the surface can readily be oxidized to create new hydroxyl radicals, which in turn boosts the efficiency of paracetamol degradation [38]. Finally, in this study, we registered that the degradation was maximal at pH 9.

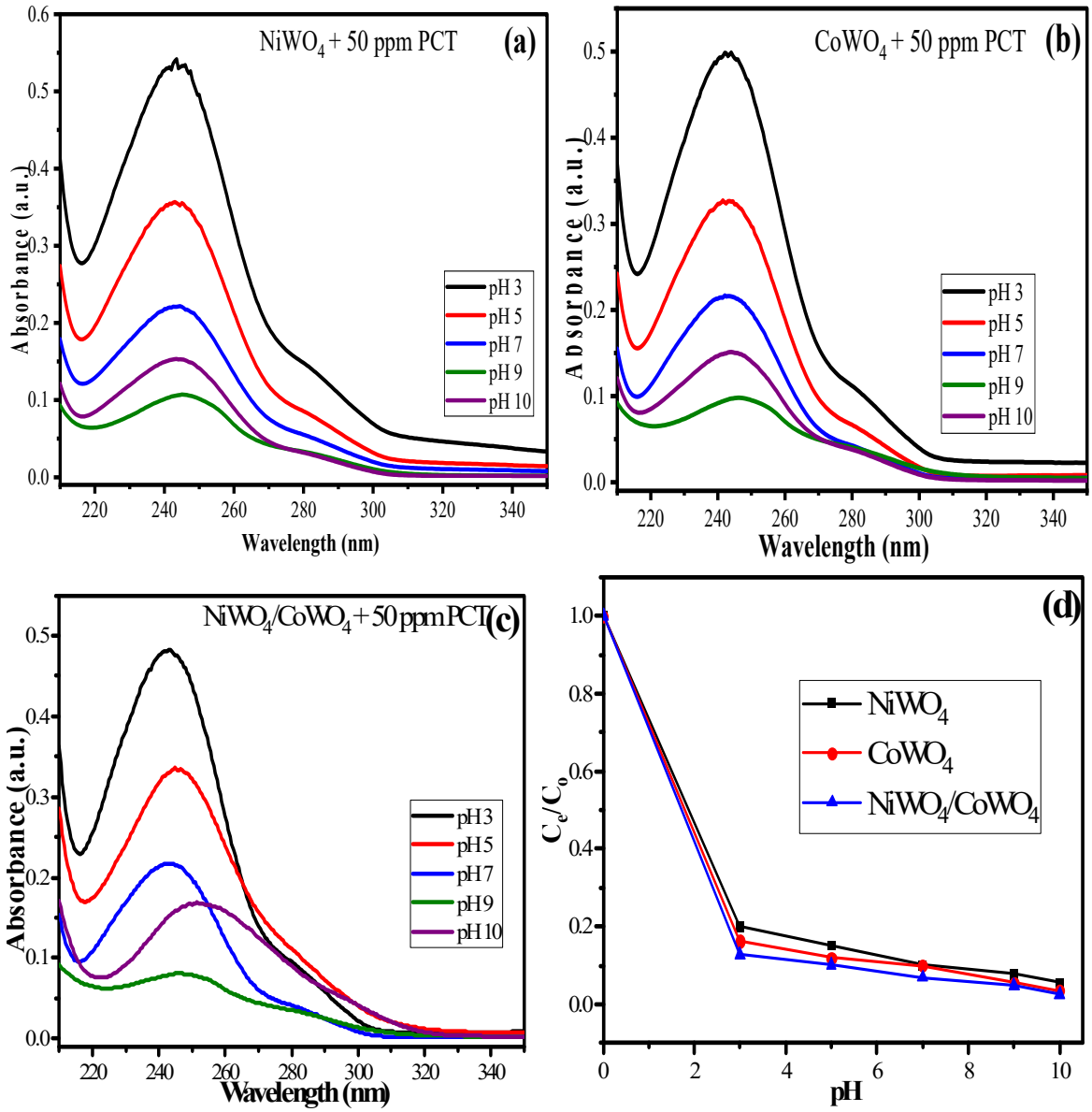

Figure 9. Effect of variable pH of the media (3–10) using 50 ppm PCT for 10 mg of (**a**) $NiWO_4$, (**b**) $CoWO_4$, (**c**) $NiWO_4/CoWO_4$ NC, and (**d**) C_e/C_o vs. pH of the medium plot.

2.2.4. Photocatalysis with Variable Irradiation Time and Kinetics of the Reaction

Photocatalytic experiments were carried out using 50 ppm paracetamol concentration, pH 9, and 10 mg of catalyst under variable irradiation time from 10 to 120 min. The results of the experiments given in Figure 10a–c show that the photocatalytic degradation of the paracetamol similarly increased with a steady increase in the irradiation time from 10 to 120 min. This trend was caused by the valence electron of a catalyst being excited from its ground state to its excited state, which produced a photoelectron by the absorption of radiation. Since there was a high density of –OH groups on the catalyst surface, when these high energy electrons coupled with them, they produced •OH radicals, which were what caused the paracetamol to photodegrade [39]. The findings in Figure 10 show that as the irradiation period increased, the degradation rate also decreased continually, and typically followed the Langmuir–Hinshelwood first-order kinetic pattern, which assumes the decomposition of the pollutant molecule at the catalyst surface to be the determining step in heterogeneous catalysis processes. The kinetic constant linked to the decomposition

and the adsorbate concentration are therefore considered to equal the product of the first-order reaction rate and the adsorbate concentration [40].

$$r = \frac{dC}{dt} = -\frac{kKC}{1 + KC} \tag{6}$$

where k is the rate constant, which is affected by light intensity, K is the catalyst adsorption constant, and C is the paracetamol concentration. (KC < 1) applies to modest low adsorption magnitudes and concentrations. Equation (7) states that Equation (6) simplifies to the first-order kinetics.

$$\frac{dC}{dt} = -kKC \tag{7}$$

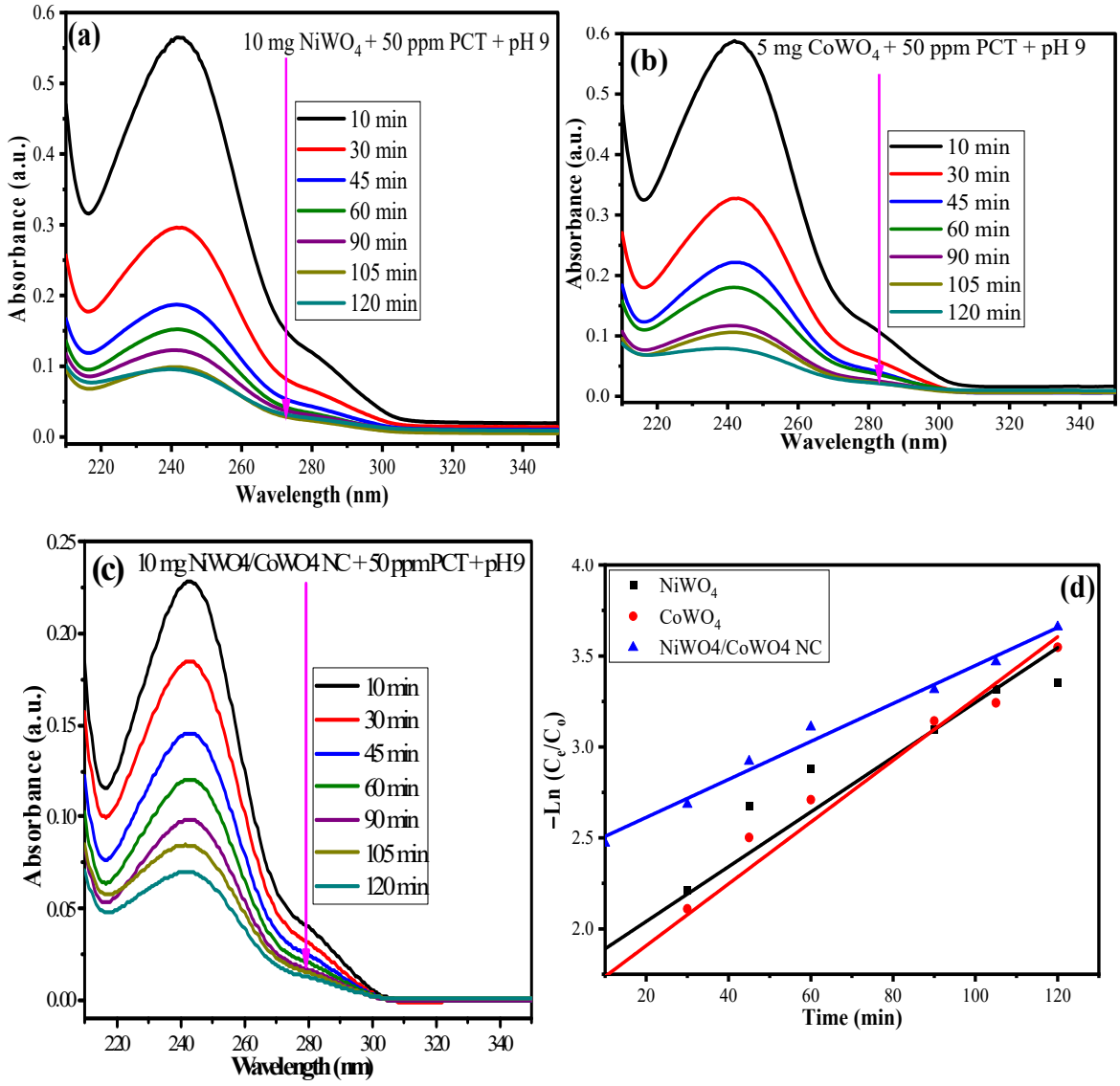

Figure 10. Effect of variable UV irradiation time (10–120 min) using 50 ppm PCT and 10 mg of (**a**) $NiWO_4$, (**b**) $CoWO_4$, (**c**) $NiWO_4/CoWO_4$ NC, and (**d**) −Ln (C_e/C_o) vs. time (min) pseudo first order plot.

Integrating and separating variables between the initial conditions t = 0 and C = C_0 at time t and if Kk = k′, where k′ is the apparent rate constant for the photocatalytic degradation.

$$\ln\left(\frac{C_0}{C}\right) = kKt = k't \tag{8}$$

Equation (3) can be plotted, and the slope represents the reaction rate constant, k′, expressed in units of min^{-1}. Given that $C = C_0/2$ in Equation (8), the half-life ($t_{1/2}$), which is an important factor in photocatalytic degradation, is the period of time needed to reduce the concentration of paracetamol by half, it may be calculated as follows by Equation (9):

$$t_{1/2} = \frac{\ln 2}{k'} \tag{9}$$

The obtained results are listed in Table 2, in which the value of apparent rate constant k′ was found to be 0.015 min^{-1} for $NiWO_4$, 0.017 min^{-1} for $CoWO_4$, and 0.019 min^{-1} for $NiWO_4/CoWO_4$ NC. The synthesized heterojunction nanocomposite exhibited a high rate of paracetamol degradation as compared to its precursors. The corresponding half-life time values were 46.20, 40.76, and 36.47 min for $NiWO_4$, $CoWO_4$, and $NiWO_4/CoWO_4$ NC. The outcomes of the kinetic studies suggested that the heterojunction formation resulted in an enhanced rate of PCT degradation as compared to pristine $NiWO_4$ and $CoWO_4$.

Table 2. Pseudo-first-order kinetic parameters for the photocatalytic degradation of paracetamol by synthesized $NiWO_4$, $CoWO_4$, and $NiWO_4/CoWO_4$ NC.

Material	k_1 (min^{-1})	R^2	$t_{1/2}$ (min)	Error
$NiWO_4$	0.015	0.95	46.20	2.31×10^{-3}
$CoWO_4$	0.017	0.98	40.76	1.46×10^{-3}
$NiWO_4/CoWO_4$	0.019	0.99	36.47	5.11×10^{-4}

2.3. Scavenging Study

The main reactive species involved in the photocatalytic process for paracetamol using $NiWO_4/CoWO_4$ NC were discovered using a variety of scavengers. Among the reactive species, the superoxide ($^{\bullet}O_2^-$), hydroxyl radical ($^{\bullet}OH$), valence band hole (h^+), and photogenerated electron (e^-) are key species on which the photodegradation of organic pollutants relies [41]. Benzoic acid (BA), acrylamide (AA), ethylenediaminetetraacetic acid (EDTA), and triphenylphosphine (TPP) were the scavengers for $^{\bullet}OH$, h^+, e^-, and $^{\bullet}O_2^-$, respectively. Figure 11 represent the results of the scavengers, which show that photogenerated (e^-) and superoxide ($^{\bullet}O_2^-$) radicals did not have any significant effect on the photocatalytic performance of the system; therefore, we can conclude that electrons do not play an important role in degradation. The degradation rate was dramatically hindered in ($^{\bullet}OH$ scavenger); as a result, it was concluded that hydroxyl radicals are the main reactive species involved in the removal of paracetamol.

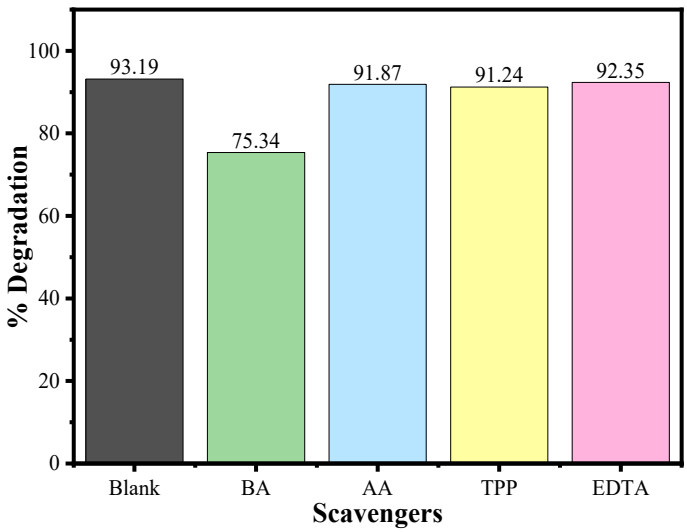

Figure 11. Photodegradation of paracetamol by $NiWO_4/CoWO_4$ NC in the presence of different scavengers.

2.4. Effect of Various Radiation and Reaction Process

Experiments were performed to observe the effects of various reaction process and radiations on the PCT degradation by $NiWO_4/CoWO_4$ NC, such as photolysis (PCT solution without catalyst under radiations), adsorption (PCT with catalyst agitated in dark), and photocatalytic reactions under UV and visible radiations. The results obtained are given in Figure 12a,b, and suggested that there is a negligible contribution from the photolysis process. PCT removal by adsorption was found to be 81%, while under visible light it was 69.27%. The maximum removal was obtained under UV light, i.e., 93.95%.

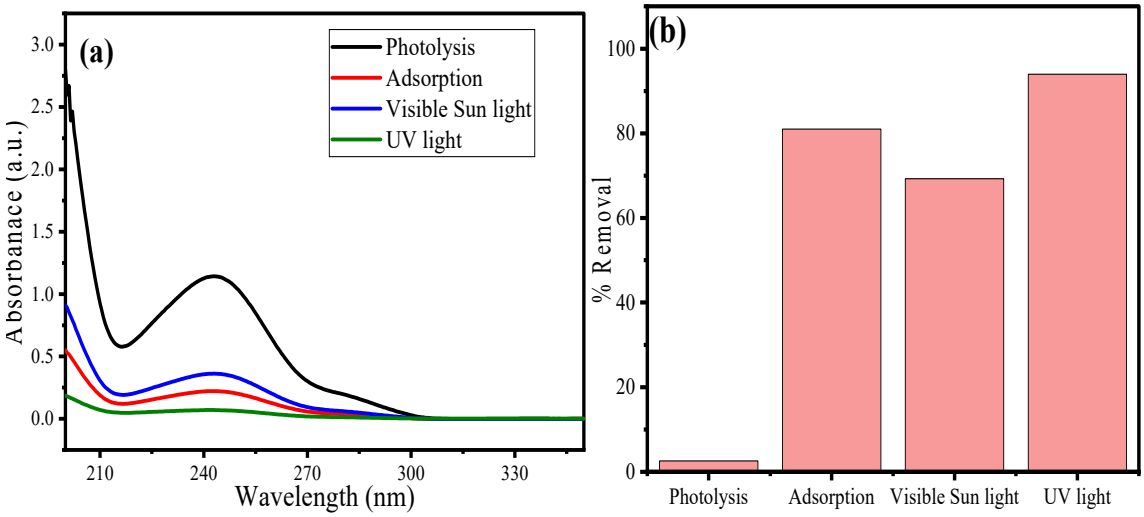

Figure 12. Effect of various reaction process and radiations on PCT degradation. (**a**) UV–Vis spectra, and (**b**) bar graph showing process vs. %PCT removal.

2.5. Comparison with Literature

Table 3 shows the photocatalytic data regarding the degradation of PCT reported in the literature as compared with the present study. It was found that no single study reported on the synthesized material in regard to PCT degradation, which confirms the novelty of this study.

Table 3. Comparison of present study with literature regarding PCT degradation.

Photocatalyst	Light Source	PCT Concentration (ppm)	Irradiation Time (min)	% Degradation	References
ZnO–Ag	Visible light	5	240	92	[42]
CuO@C	LED light	5	60	95	[43]
g-C_3N_4/(101)-(001)-TiO_2	300 W xenon lamp	10	300	69.49	[44]
$Cu_2O/WO_3/TiO_2$	Solar light	1	60	92.50	[45]
Bi_2WO_6-CNP-TiO_2	LCS-100 W solar simulator	5	180	84	[46]
$NiWO_4/CoWO_4$ NC	UV light	50	120	97.42	Present study

3. Methods and Materials

3.1. Chemicals and Reagents

Acetaminophen ($CH_3CONHC_6H_4OH$, Analytical grade, 99%), sodium tungstate dihydrate ($Na_2WO_4{\cdot}2H_2O$, 96%, laboratory reagent) were purchased from Merck, Darmstadt, Germany), Nickel nitrate hexahydrate (Ni $(NO_3)_2{\cdot}6H_2O$ 98%), cobalt nitrate hexahydrate (Co $(NO_3)_2{\cdot}6H_2O$, 98%) were supplied by Thermo Fisher Scientific, Dreieich, Germany.

General purpose reagent such as ammonia solution (NH_4OH, 25%, extra pure), and ethanol (C_2H_5OH, 96%, ACS grade) were supplied by Alfa Aesar, Kandel, Germany. The obtained chemicals were employed directly without any further processing, and the solutions were made using distilled water.

3.2. Synthesis of Nickel Tungstate ($NiWO_4$) Nanomaterials

The hydrothermal process was taken into consideration for synthesis of the nanomaterials reported elsewhere [20,23]. Ni $(NO_3)_2{\cdot}6H_2O$ (3 mmol) and $Na_2WO_4{\cdot}2H_2O$ (5 mmol) were taken individually in 25 mL of distilled water while being stirred magnetically for 15 min for complete dissolution. The two aqueous solutions above were then combined using magnetic stirring for 30 min at room temperature. The mixture was then transferred into 80 mL Teflon-lined steel autoclave and heated for 18 h at 180 °C in a convection oven. After the completion of the reaction, the autoclave was left to cool normally at room temperature and the precipitate was collected through centrifugation. The material was washed with distilled water and ethanol and then dehydrated in a vacuum oven at 80 °C for 5 h. The material was finally calcined at 600 °C for 4 h and stored in desiccator for further characterization and applications. In a similar fashion, $CoWO_4$ (3 mmol) was prepared, and the heterojunction nanocomposite was prepared by adding 3 mmol of Ni $(NO_3)_2{\cdot}6H_2O$ and 1.5 mmol of Co $(NO_3)_2{\cdot}6H_2O$ with 5 mmol of $Na_2WO_4{\cdot}2H_2O$.

3.3. Characterization of the Synthesized Nanomaterials

Fourier Transform Infrared Spectroscopy (FTIR) system spectrum BX (Perkin Elmer, Akron, OH, USA) which operates in the 4400–400 cm^{-1} range, was used to explore the various types of bonding and functional group contained in the material. The XRD diffractometer, (A Rigaku Ultima) (Rigaku, Austin, TX, USA) was employed to identify the crystalline structure, crystalline size and lattice phase of synthesized nanoparticles. SEM integrated with EDX (SEM; JEOL GSM 6510LV, Tokyo, Japan) was used to examine the surface morphology of the material in order to learn more about its elemental composition as well as the chemical composition and homogeneity of its manufactured $NiWO_4/CoWO_4$ NC. Through the use of a transmission electron microscope, the particle size and distribution were evaluated (TEM, TEM: JEM 2100, Tokyo, Japan). UV-1800 spectrophotometer (SHIMADZU, Kyoto, Japan), was used for the analysis of synthesized nanoparticles before and after the photocatalytic reaction in the range of 200–700 nm. The chemical state of the elements in the synthesized material was analyzed by X-ray photoelectron spectroscopy (XPS, PHI 5000 Versa Probe III, Physical Electronics, Chanhassen, MN, USA).

3.4. Photocatalysis Experiment

The photocatalytic technique was utilized to observe the degradation of paracetamol under ultraviolet radiation. Accordingly, 20 mL aliquots of variable concentration of paracetamol (5–60 ppm), solution pH (3–10), and (5–20 mg) of catalyst were subjected to magnetic stirring time (10–120 min) under mercury lamp irradiation using a photocatalytic reactor. The percentage of paracetamol (%) that was degraded in an aqueous solution was varied to determine the photocatalyst's effectiveness. The UV–Vis spectrophotometer was used to examine the paracetamol effluents following the photocatalytic reaction at the highest absorption wavelength (λ_{max} = 243 nm). Equation (10) was used to assess the percentage of paracetamol degradation.

$$\%\ \text{Degradation} = \frac{C_o - C_t}{C_o} \times 100 \tag{10}$$

where C_o is the initial paracetamol concentration and C_t is the concentrations of paracetamol after the photocatalysis reaction.

4. Conclusions

The present study considers the use of a hydrothermal reaction to synthesize $NiWO_4$, $CoWO_4$, and their heterojunction $NiWO_4/CoWO_4$ nanocomposite materials. The synthesized materials were subjected to various structural, morphological, and optical tests to confirm their correct formation and to test the hypothesis of the research. The FTIR analysis confirmed the formation of the heterojunction through electrostatic interactions between CoO_6 and NiO_6 octahedra in the corners with a WO_6^{6-} frame in a wolframite monoclinic lattice. The outcomes of the FTIR studies were further supported by the XRD studies, with an increase in dislocation density to 2.75 in $NiWO_4/CoWO_4$ from 1.35 in $CoWO_4$ and 2.03 $NiWO_4$. The heterojunction formation also resulted in a contraction in Scherer particle size to 19.07 nm for $NiWO_4/CoWO_4$, which was also found to be in close agreement with the TEM analysis. The SEM–TEM analysis resulted in the formation of a mitigated wolframite monoclinic structure for the synthesized heterojunction nanocomposite, with an average particle size of around 20 nm. The EDX analysis confirmed the presence of Ni, Co, W, and O in the synthesized nanocomposite material. The UV–Vis spectroscopy revealed the values of the energy band gap for $NiWO_4$ (3.04 eV), $CoWO_4$ (2.32 eV), and $NiWO_4/CoWO_4$ (1.14 eV), which supported the conclusion that the formation of heterojunction results in a contraction in the energy bandgap. The synthesized materials were explored as photocatalysts for the degradation of the paracetamol drug under UV light radiation. The optimized operational parameters were found be to 120 min irradiation time, pH 9, and 10 mg of catalyst dose with 50 ppm of paracetamol. At optimized conditions, the photocatalytic efficiencies of the synthesized nanocatalysts were calculated as 96.50% for $NiWO_4$, 97.12% for $CoWO_4$, and 97.42% for $NiWO_4/CoWO_4$ NC. The values of the apparent rate constant obtained from the Langmuir–Hinshelwood model were found to be 0.015 min^{-1} for $NiWO_4$, 0.017 min^{-1} for $CoWO_4$, and 0.019 min^{-1} for $NiWO_4/CoWO_4$ NC. The high values of the rate constant suggested the high photocatalytic efficiency of the heterojunction NC $NiWO_4/CoWO_4$. The outcomes of this study suggest that the heterojunction $NiWO_4/CoWO_4$ NC can be used for photocatalytic degradation of other pharmaceutical pollutants with high efficiency.

Author Contributions: Conceptualization, F.A.A., H.S.A. and A.E.M.; methodology, I.H., F.A.A. and H.S.A.; software, I.H., A.E.M. and F.A.A.; validation, I.H., F.A.A. and H.S.A.; formal analysis, A.A.A. and W.S.A.-N.; investigation, A.A.A. and W.S.A.-N.; resources A.A.A., W.S.A.-N. and I.H.; data curation, I.H., A.E.M. and H.S.A.; writing—original draft preparation, A.A.A. and W.S.A.-N.; writing—review and editing, I.H. and F.A.A.; visualization, H.S.A., I.H. and A.E.M.; supervision, F.A.A. and H.S.A.; project administration, F.A.A.; funding acquisition, F.A.A. All authors have read and agreed to the published version of the manuscript.

Funding: This research received no external funding.

Data Availability Statement: Data is contained within the article.

Acknowledgments: The authors extend their appreciation to the deputyship of Research and Innovation, Ministry of Education in Saudi Arabia for funding this research work through project number (IFKSURG-2-1329).

Conflicts of Interest: The authors declare that there is no conflict of interest related to this research, and the paper has not been submitted to any other journal simultaneously.

References

1. Jóźwiak-Bebenista, M.; Nowak, J.Z. Paracetamol: Mechanism of action, applications and safety concern. *Acta Pol. Pharm.* **2014**, *71*, 11–23. [PubMed]
2. Klotz, U. Paracetamol (acetaminophen)—A popular and widely used nonopioid analgesic. *Arzneimittelforschung* **2012**, *62*, 355–359. [CrossRef] [PubMed]
3. Wexler, P.; Anderson, B.D.; Gad, S.C.; Hakkinen, P.B.; Kamrin, M.; de Peyster, A.; Locey, B.; Pope, C.; Mehendale, H.M.; Shugart, L.R.; et al. *Encyclopedia of Toxicology*; Academic Press: Cambridge, MA, USA, 2005; Volume 1.

4. Galani, A.; Alygizakis, N.; Aalizadeh, R.; Kastritis, E.; Dimopoulos, M.A.; Thomaidis, N.S. Patterns of Pharmaceuticals Use during the First Wave of COVID-19 Pandemic in Athens, Greece as Revealed by Wastewater-Based Epidemiology. *Sci. Total Environ.* **2021**, *798*, 149014. [CrossRef] [PubMed]
5. Karungamye, P.N. Methods used for removal of pharmaceuticals from wastewater: A review. *Appl. J. Environ. Eng. Sci.* **2020**, *6*, 412–428.
6. Choina, J.; Kosslick, H.; Fischer, C.; Flechsig, G.U.; Frunza, L.; Schulz, A. Photocatalytic decomposition of pharmaceutical ibuprofen pollutions in water over titania catalyst. *Appl. Catal. B Environ.* **2013**, *129*, 589–598. [CrossRef]
7. Shakir, M.; Faraz, M.; Sherwani, M.A.; Al-Resayes, S. Photocatalytic degradation of the Paracetamol drug using Lanthanum doped ZnO nanoparticles and their in-vitro cytotoxicity assay. *J. Lumin.* **2016**, *176*, 159–167. [CrossRef]
8. Amrane, A.; Rajendran, S.; Nguyen, T.A.; Assadi, A.; Sharoba, A. *Nanotechnology in the Beverage Industry: Fundamentals and Applications*; Elsevier: Amsterdam, The Netherlands, 2020.
9. Bibi, S.; Ahmad, A.; Anjum, M.A.R.; Haleem, A.; Siddiq, M.; Shah, S.S.; Kahtani, A. Photocatalytic Degradation of Malachite Green and Methylene Blue over Reduced Graphene Oxide (RGO) Based Metal Oxides (RGO-Fe_3O_4/TiO_2) Nanocomposite under UV-Visible Light Irradiation. *J. Environ. Chem. Eng.* **2021**, *9*, 105580. [CrossRef]
10. Shah, L.A.; Malik, T.; Siddiq, M.; Haleem, A.; Sayed, M.; Naeem, A. TiO_2 Nanotubes Doped Poly (Vinylidene Fluoride) Polymer Membranes (PVDF/TNT) for Efficient Photocatalytic Degradation of Brilliant Green Dye. *J. Environ. Chem. Eng.* **2019**, *7*, 103291. [CrossRef]
11. Hayat, M.; Shah, A.; Hakeem, M.K.; Irfan, M.; Haleem, A.; Khan, S.B.; Shah, I. A Designed Miniature Sensor for the Trace Level Detection and Degradation Studies of the Toxic Dye Rhodamine B. *RSC Adv.* **2022**, *12*, 15658–15669. [CrossRef]
12. Hayat, M.; Shah, A.; Nisar, J.; Shah, I.; Haleem, A.; Ashiq, M.N. A Novel Electrochemical Sensing Platform for the Sensitive Detection and Degradation Monitoring of Methylene Blue. *Catalysts* **2022**, *12*, 306. [CrossRef]
13. Tahir, M.B.; Rafique, M.; Nabi, G.; Shafiq, F. Photocatalytic nanomaterials for the removal of pharmaceuticals. In *Nanotechnology and Photocatalysis for Environmental Applications*; Elsevier: Amsterdam, The Netherlands, 2020; pp. 191–202.
14. Ismail, W.N.W.; Mokhtar, S.U. Various methods for removal, treatment, and detection of emerging water contaminants. In *Emerging Contaminants*; IntechOpen: London, UK, 2020.
15. Mirzaei, A.; Chen, Z.; Haghighat, F.; Yerushalmi, L. Removal of pharmaceuticals and endocrine disrupting compounds from water by zinc oxide-based photocatalytic degradation: A review. *Sustain. Cities Soc.* **2016**, *27*, 407–418. [CrossRef]
16. Massima Mouele, E.S.; Tijani, J.O.; Badmus, K.O.; Pereao, O.; Babajide, O.; Zhang, C.; Shao, T.; Sosnin, E.; Tarasenko, V.; Fatoba, O.O.; et al. Removal of pharmaceutical residues from water and wastewater using dielectric barrier discharge methods—A review. *Int. J. Environ. Res. Public Health* **2021**, *18*, 1683. [CrossRef] [PubMed]
17. Nor, N.A.M.; Jaafar, J.; Othman, M.H.D.; Rahman, M.A. A review study of nanofibers in photocatalytic process for wastewater treatment. *J. Teknol.* **2013**, *65*, 2335. [CrossRef]
18. Montini, T.; Gombac, V.; Hameed, A.; Felisari, L.; Adami, G.; Fornasiero, P. Synthesis, characterization and photocatalytic performance of transition metal tungstates. *Chem. Phys. Lett.* **2010**, *498*, 113–119. [CrossRef]
19. Chukwuike, V.I.; Sankar, S.S.; Kundu, S.; Barik, R.C. Nanostructured cobalt tungstate ($CoWO_4$): A highly promising material for fabrication of protective oxide film on copper in chloride medium. *J. Electrochem. Soc.* **2019**, *166*, C631. [CrossRef]
20. Zawawi, S.M.; Yahya, R.; Hassan, A.; Mahmud, H.N.M.; Daud, M.N. Structural and optical characterization of metal tungstates (MWO_4; M = Ni, Ba, Bi) synthesized by a sucrose-templated method. *Chem. Cent. J.* **2013**, *7*, 80. [CrossRef]
21. Sun, Y.; Wang, X.; Fu, Q.; Pan, C. Construction of Direct Z-Scheme Heterojunction NiFe-Layered Double Hydroxide (LDH)/$Zn_{0.5}Cd_{0.5}S$ for Photocatalytic H_2 Evolution. *ACS Appl. Mater. Interfaces* **2021**, *13*, 39331–39340. [CrossRef]
22. Liao, Y.; Wang, G.; Wang, J.; Wang, K.; Yan, S.; Su, Y. Nitrogen Vacancy Induced in Situ G-C_3N_4 p-n Homojunction for Boosting Visible Light-Driven Hydrogen Evolution. *J. Colloid Interface Sci.* **2021**, *587*, 110–120. [CrossRef]
23. Güy, N.; Atacan, K.; Özacar, M. Rational Construction of P-n-p CuO/CdS/$CoWO_4$ S-Scheme Heterojunction with Influential Separation and Directional Transfer of Interfacial Photocarriers for Boosted Photocatalytic H_2 Evolution. *Renew. Energy* **2022**, *195*, 107–120. [CrossRef]
24. Jothivenkatachalam, K.; Prabhu, S.; Nithya, A.; Chandra Mohan, S.; Jeganathan, K. Solar, visible and UV light photocatalytic activity of $CoWO_4$ for the decolourization of methyl orange. *Desalination Water Treat.* **2015**, *54*, 3134–3145. [CrossRef]
25. Srirapu, V.K.V.P.; Kumar, A.; Srivastava, P.; Singh, R.N.; Sinha, A.S.K. Nanosized $CoWO_4$ and $NiWO_4$ as efficient oxygen-evolving electrocatalysts. *Electrochim. Acta* **2016**, *209*, 75–84. [CrossRef]
26. Taneja, P.; Sharma, S.; Umar, A.; Mehta, S.K.; Ibhadon, A.O.; Kansal, S.K. Visible-light driven photocatalytic degradation of brilliant green dye based on cobalt tungstate ($CoWO_4$) nanoparticles. *Mater. Chem. Phys.* **2018**, *211*, 335–342. [CrossRef]
27. Kumaresan, A.; Arun, A.; Kalpana, V.; Vinupritha, P.; Sundaravadivel, E. Polymer-supported $NiWO_4$ nanocomposites for visible light degradation of toxic dyes. *J. Mater. Sci. Mater. Electron.* **2022**, *33*, 9660–9668. [CrossRef]
28. Ahmadi, F.; Rahimi-Nasrabadi, M.; Fosooni, A.; Daneshmand, M. Synthesis and application of $CoWO_4$ nanoparticles for degradation of methyl orange. *J. Mater. Sci. Mater. Electron.* **2016**, *27*, 9514–9519. [CrossRef]
29. Li, X.; Li, X.; Li, Z.; Wang, J.; Zhang, J. WS_2 Nanoflakes Based Selective Ammonia Sensors at Room Temperature. *Sens. Actuators B Chem.* **2017**, *240*, 273–277. [CrossRef]
30. Wang, G.; Ling, Y.; Wang, H.; Yang, X.; Wang, C.; Zhang, J.Z.; Li, Y. Hydrogen-Treated WO_3 Nanoflakes Show Enhanced Photostability. *Energy Environ. Sci.* **2012**, *5*, 6180–6187. [CrossRef]

31. Zhu, J.; Li, W.; Li, J.; Li, Y.; Hu, H.; Yang, Y. Photoelectrochemical Activity of $NiWO_4/WO_3$ Heterojunction Photoanode under Visible Light Irradiation. *Electrochim. Acta* **2013**, *112*, 191–198. [CrossRef]
32. Xu, S.; Li, X.; Yang, Z.; Wang, T.; Jiang, W.; Yang, C.; Wang, S.; Hu, N.; Wei, H.; Zhang, Y.; et al. Nanofoaming to Boost the Electrochemical Performance of Ni@Ni$(OH)_2$ Nanowires for Ultrahigh Volumetric Supercapacitors. *ACS Appl. Mater. Interfaces* **2016**, *8*, 27868–27876. [CrossRef]
33. Alshehri, S.M.; Ahmed, J.; Ahamad, T.; Arunachalam, P.; Ahmad, T.; Khan, A. Bifunctional Electro-Catalytic Performances of $CoWO_4$ Nanocubes for Water Redox Reactions (OER/ORR). *RSC Adv.* **2017**, *7*, 45615–45623. [CrossRef]
34. Liu, Y.; Wan, K.; Deng, N.; Wu, F. Photodegradation of paracetamol in montmorillonite KSF suspension. *React. Kinet. Mech. Catal.* **2010**, *99*, 493–502. [CrossRef]
35. Vaiano, V.; Sacco, O.; Matarangolo, M. Photocatalytic degradation of paracetamol under UV irradiation using TiO_2-graphite composites. *Catal. Today* **2018**, *315*, 230–236. [CrossRef]
36. Hu, C.; Xu, J.; Zhu, Y.; Chen, A.; Bian, Z.; Wang, H. Morphological effect of $BiVO_4$ catalysts on degradation of aqueous paracetamol under visible light irradiation. *Environ. Sci. Pollut. Res.* **2016**, *23*, 18421–18428. [CrossRef]
37. Harimisa, G.E.; Mustapha, M.H.; Masudi, A.; Jusoh, N.C.; Tan, L.S. March. Enhanced Degradation Rates of Paracetamol in Aqueous Solution using Silver Doped Durio Zibethinus Husk Catalyst. In *IOP Conference Series: Materials Science and Engineering*; IOP Publishing: Bristol, UK, 2020; Volume 808, p. 012014.
38. Borges, M.E.; García, D.M.; Hernández, T.; Ruiz-Morales, J.C.; Esparza, P. Supported photocatalyst for removal of emerging contaminants from wastewater in a continuous packed-bed photoreactor configuration. *Catalysts* **2015**, *5*, 77–87. [CrossRef]
39. Hasan, I.; Bassi, A.; Alharbi, K.H.; BinSharfan, I.I.; Khan, R.A.; Alslame, A. Sonophotocatalytic degradation of malachite green by nanocrystalline chitosan-ascorbic Acid@ $NiFe_2O_4$ spinel ferrite. *Coatings* **2020**, *10*, 1200. [CrossRef]
40. Lozano-Morales, S.A.; Morales, G.; López Zavala, M.Á.; Arce-Sarria, A.; Machuca-Martínez, F. Photocatalytic treatment of paracetamol using TiO_2 nanotubes: Effect of pH. *Processes* **2019**, *7*, 319. [CrossRef]
41. Mao, S.; Bao, R.; Fang, D.; Yi, J. Facile synthesis of Ag/AgX (X = Cl, Br) with enhanced visible-light-induced photocatalytic activity by ultrasonic spray pyrolysis method. *Adv. Powder Technol.* **2018**, *29*, 2670–2677. [CrossRef]
42. Al-Gharibi, M.A.; Kyaw, H.H.; Al-Sabahi, J.N.; Zar Myint, M.T.; Al-Sharji, Z.A.; Al-Abri, M.Z. Silver Nanoparticles Decorated Zinc Oxide Nanorods Supported Catalyst for Photocatalytic Degradation of Paracetamol. *Mater. Sci. Semicond. Process.* **2021**, *134*, 105994. [CrossRef]
43. Abdelhaleem, A.; Abdelhamid, H.N.; Ibrahim, M.G.; Chu, W. Photocatalytic Degradation of Paracetamol Using Photo-Fenton-like Metal-Organic Framework-Derived CuO@C under Visible LED. *J. Clean. Prod.* **2022**, *379*, 134571. [CrossRef]
44. Sun, J.; Deng, L.; Sun, J.; Shen, T.; Wang, X.; Zhao, R.; Zhang, Y.; Wang, B. Construction of a Double Heterojunction between Graphite Carbon Nitride and Anatase TiO_2 with Co-Exposed (101) and (001) Faces for Enhanced Photocatalytic Degradation. *RSC Adv.* **2022**, *12*, 20206–20216. [CrossRef]
45. Chau, J.H.F.; Lai, C.W.; Leo, B.F.; Juan, J.C.; Johan, M.R. Advanced Photocatalytic Degradation of Acetaminophen Using $Cu_2O/WO_3/TiO_2$ Ternary Composite under Solar Irradiation. *Catal. Commun.* **2022**, *163*, 106396. [CrossRef]
46. Mahhumane, N.; Cele, L.M.; Muzenda, C.; Nkwachukwu, O.V.; Koiki, B.A.; Arotiba, O.A. Enhanced Visible Light-Driven Photoelectrocatalytic Degradation of Paracetamol at a Ternary z-Scheme Heterojunction of Bi_2WO_6 with Carbon Nanoparticles and TiO_2 Nanotube Arrays Electrode. *Nanomaterials* **2022**, *12*, 2467. [CrossRef] [PubMed]